Amplitude analysis of the $D^+ \to K_S^0 \pi^+ \pi^0$ Dalitz plot

M. Ablikim,[1] M. N. Achasov,[8,*] X. C. Ai,[1] O. Albayrak,[4] M. Albrecht,[3] D. J. Ambrose,[41] F. F. An,[1] Q. An,[42] J. Z. Bai,[1] R. Baldini Ferroli,[19a] Y. Ban,[28] J. V. Bennett,[18] M. Bertani,[19a] J. M. Bian,[40] E. Boger,[21,†] O. Bondarenko,[22] I. Boyko,[21] S. Braun,[37] R. A. Briere,[4] H. Cai,[47] X. Cai,[1] O. Cakir,[36a] A. Calcaterra,[19a] G. F. Cao,[1] S. A. Cetin,[36b] J. F. Chang,[1] G. Chelkov,[21,†] G. Chen,[1] H. S. Chen,[1] J. C. Chen,[1] M. L. Chen,[1] S. J. Chen,[26] X. Chen,[1] X. R. Chen,[23] Y. B. Chen,[1] H. P. Cheng,[16] X. K. Chu,[28] Y. P. Chu,[1] D. Cronin-Hennessy,[40] H. L. Dai,[1] J. P. Dai,[1] D. Dedovich,[21] Z. Y. Deng,[1] A. Denig,[20] I. Denysenko,[21] M. Destefanis,[45a,45c] W. M. Ding,[30] Y. Ding,[24] C. Dong,[27] J. Dong,[1] L. Y. Dong,[1] M. Y. Dong,[1] S. X. Du,[49] J. Z. Fan,[35] J. Fang,[1] S. S. Fang,[1] Y. Fang,[1] L. Fava,[45b,45c] C. Q. Feng,[42] C. D. Fu,[1] O. Fuks,[21,†] Q. Gao,[1] Y. Gao,[35] C. Geng,[42] K. Goetzen,[9] W. X. Gong,[1] W. Gradl,[20] M. Greco,[45a,45c] M. H. Gu,[1] Y. T. Gu,[11] Y. H. Guan,[1] A. Q. Guo,[27] L. B. Guo,[25] T. Guo,[25] Y. P. Guo,[20] Y. L. Han,[1] F. A. Harris,[39] K. L. He,[1] M. He,[1] Z. Y. He,[27] T. Held,[3] Y. K. Heng,[1] Z. L. Hou,[1] C. Hu,[25] H. M. Hu,[1] J. F. Hu,[37] T. Hu,[1] G. M. Huang,[5] G. S. Huang,[42] H. P. Huang,[47] J. S. Huang,[14] L. Huang,[1] X. T. Huang,[30] Y. Huang,[26] T. Hussain,[44] C. S. Ji,[42] Q. Ji,[1] Q. P. Ji,[27] X. B. Ji,[1] X. L. Ji,[1] L. L. Jiang,[1] L. W. Jiang,[47] X. S. Jiang,[1] J. B. Jiao,[30] Z. Jiao,[16] D. P. Jin,[1] S. Jin,[1] T. Johansson,[46] N. Kalantar-Nayestanaki,[22] X. L. Kang,[1] X. S. Kang,[27] M. Kavatsyuk,[22] B. Kloss,[20] B. Kopf,[3] M. Kornicer,[39] W. Kuehn,[37] A. Kupsc,[46] W. Lai,[1] J. S. Lange,[37] M. Lara,[18] P. Larin,[13] M. Leyhe,[3] C. H. Li,[1] Cheng Li,[42] Cui Li,[42] D. Li,[17] D. M. Li,[49] F. Li,[1] G. Li,[1] H. B. Li,[1] J. C. Li,[1] K. Li,[12] K. Li,[30] Lei Li,[1] P. R. Li,[38] Q. J. Li,[1] T. Li,[30] W. D. Li,[1] W. G. Li,[1] X. L. Li,[30] X. N. Li,[1] X. Q. Li,[27] Z. B. Li,[34] H. Liang,[42] Y. F. Liang,[32] Y. T. Liang,[37] D. X. Lin,[13] B. J. Liu,[1] C. L. Liu,[4] C. X. Liu,[1] F. H. Liu,[31] Fang Liu,[1] Feng Liu,[5] H. B. Liu,[11] H. H. Liu,[15] H. M. Liu,[1] J. Liu,[1] J. P. Liu,[47] K. Liu,[35] K. Y. Liu,[24] P. L. Liu,[30] Q. Liu,[38] S. B. Liu,[42] X. Liu,[23] Y. B. Liu,[27] Z. A. Liu,[1] Zhiqiang Liu,[1] Zhiqing Liu,[20] H. Loehner,[22] X. C. Lou,[1,‡] G. R. Lu,[14] H. J. Lu,[16] H. L. Lu,[1] J. G. Lu,[1] X. R. Lu,[38] Y. Lu,[1] Y. P. Lu,[1] C. L. Luo,[25] M. X. Luo,[48] T. Luo,[39] X. L. Luo,[1] M. Lv,[1] F. C. Ma,[24] H. L. Ma,[1] Q. M. Ma,[1] S. Ma,[1] T. Ma,[1] X. Y. Ma,[1] F. E. Maas,[13] M. Maggiora,[45a,45c] Q. A. Malik,[44] Y. J. Mao,[28] Z. P. Mao,[1] J. G. Messchendorp,[22] J. Min,[1] T. J. Min,[1] R. E. Mitchell,[18] X. H. Mo,[1] Y. J. Mo,[5] H. Moeini,[22] C. Morales Morales,[13] K. Moriya,[18] N. Yu. Muchnoi,[8,*] H. Muramatsu,[40] Y. Nefedov,[21] I. B. Nikolaev,[8,*] Z. Ning,[1] S. Nisar,[7] X. Y. Niu,[1] S. L. Olsen,[29] Q. Ouyang,[1] S. Pacetti,[19b] M. Pelizaeus,[3] H. P. Peng,[42] K. Peters,[9] J. L. Ping,[25] R. G. Ping,[1] R. Poling,[40] N. Qin,[47] M. Qi,[26] S. Qian,[1] C. F. Qiao,[38] L. Q. Qin,[30] X. S. Qin,[1] Y. Qin,[28] Z. H. Qin,[1] J. F. Qiu,[1] K. H. Rashid,[44] C. F. Redmer,[20] M. Ripka,[20] G. Rong,[1] X. D. Ruan,[11] A. Sarantsev,[21,§] K. Schoenning,[46] S. Schumann,[20] W. Shan,[28] M. Shao,[42] C. P. Shen,[2] X. Y. Shen,[1] H. Y. Sheng,[1] M. R. Shepherd,[18] W. M. Song,[1] X. Y. Song,[1] S. Spataro,[45a,45c] B. Spruck,[37] G. X. Sun,[1] J. F. Sun,[14] S. S. Sun,[1] Y. J. Sun,[42] Y. Z. Sun,[1] Z. J. Sun,[1] Z. T. Sun,[42] C. J. Tang,[32] X. Tang,[1] I. Tapan,[36c] E. H. Thorndike,[41] D. Toth,[40] M. Ullrich,[37] I. Uman,[36b] G. S. Varner,[39] B. Wang,[27] D. Wang,[28] D. Y. Wang,[28] K. Wang,[1] L. L. Wang,[1] L. S. Wang,[1] M. Wang,[30] P. Wang,[1] P. L. Wang,[1] Q. J. Wang,[1] S. G. Wang,[28] W. Wang,[1] X. F. Wang,[35] Y. D. Wang,[19a] Y. F. Wang,[1] Y. Q. Wang,[20] Z. Wang,[1] Z. G. Wang,[1] Z. H. Wang,[42] Z. Y. Wang,[1] D. H. Wei,[10] J. B. Wei,[28] P. Weidenkaff,[20] S. P. Wen,[1] M. Werner,[37] U. Wiedner,[3] M. Wolke,[46] L. H. Wu,[1] N. Wu,[1] Z. Wu,[1] L. G. Xia,[35] Y. Xia,[17] D. Xiao,[1] Z. J. Xiao,[25] Y. G. Xie,[1] Q. L. Xiu,[1] G. F. Xu,[1] L. Xu,[1] Q. J. Xu,[12] Q. N. Xu,[38] X. P. Xu,[33] Z. Xue,[1] L. Yan,[42] W. B. Yan,[42] W. C. Yan,[42] Y. H. Yan,[17] H. X. Yang,[1] L. Yang,[47] Y. Yang,[5] Y. X. Yang,[10] H. Ye,[1] M. Ye,[1] M. H. Ye,[6] B. X. Yu,[1] C. X. Yu,[27] H. W. Yu,[28] J. S. Yu,[23] S. P. Yu,[30] C. Z. Yuan,[1] W. L. Yuan,[26] Y. Yuan,[1] A. A. Zafar,[44] A. Zallo,[19a] S. L. Zang,[26] Y. Zeng,[17] B. X. Zhang,[1] B. Y. Zhang,[1] C. Zhang,[26] C. B. Zhang,[17] C. C. Zhang,[1] D. H. Zhang,[1] H. H. Zhang,[34] H. Y. Zhang,[1] J. J. Zhang,[1] J. Q. Zhang,[1] J. W. Zhang,[1] J. Y. Zhang,[1] J. Z. Zhang,[1] S. H. Zhang,[1] X. J. Zhang,[1] X. Y. Zhang,[30] Y. Zhang,[1] Y. H. Zhang,[1] Z. H. Zhang,[5] Z. P. Zhang,[42] Z. Y. Zhang,[47] G. Zhao,[1] J. W. Zhao,[1] Lei Zhao,[42] Ling Zhao,[1] M. G. Zhao,[27] Q. Zhao,[1] Q. W. Zhao,[1] S. J. Zhao,[49] T. C. Zhao,[1] X. H. Zhao,[26] Y. B. Zhao,[1] Z. G. Zhao,[42] A. Zhemchugov,[21,†] B. Zheng,[43] J. P. Zheng,[1] Y. H. Zheng,[38] B. Zhong,[25] L. Zhou,[1] Li Zhou,[27] X. Zhou,[47] X. K. Zhou,[38] X. R. Zhou,[42] X. Y. Zhou,[1] K. Zhu,[1] K. J. Zhu,[1] X. L. Zhu,[35] Y. C. Zhu,[42] Y. S. Zhu,[1] Z. A. Zhu,[1] J. Zhuang,[1] B. S. Zou,[1] and J. H. Zou,[1]

(BESIII Collaboration)

[1]*Institute of High Energy Physics, Beijing 100049, People's Republic of China*
[2]*Beihang University, Beijing 100191, People's Republic of China*
[3]*Bochum Ruhr-University, D-44780 Bochum, Germany*
[4]*Carnegie Mellon University, Pittsburgh, Pennsylvania 15213, USA*
[5]*Central China Normal University, Wuhan 430079, People's Republic of China*
[6]*China Center of Advanced Science and Technology, Beijing 100190, People's Republic of China*
[7]*COMSATS Institute of Information Technology, Lahore, Defence Road, Off Raiwind Road, 54000 Lahore, Pakistan*
[8]*G.I. Budker Institute of Nuclear Physics SB RAS (BINP), Novosibirsk 630090, Russia*
[9]*GSI Helmholtzcentre for Heavy Ion Research GmbH, D-64291 Darmstadt, Germany*
[10]*Guangxi Normal University, Guilin 541004, People's Republic of China*
[11]*GuangXi University, Nanning 530004, People's Republic of China*

[12]Hangzhou Normal University, Hangzhou 310036, People's Republic of China

[13]Helmholtz Institute Mainz, Johann-Joachim-Becher-Weg 45, D-55099 Mainz, Germany

[14]Henan Normal University, Xinxiang 453007, People's Republic of China

[15]Henan University of Science and Technology, Luoyang 471003, People's Republic of China

[16]Huangshan College, Huangshan 245000, People's Republic of China

[17]Hunan University, Changsha 410082, People's Republic of China

[18]Indiana University, Bloomington, Indiana 47405, USA

[19a]INFN Laboratori Nazionali di Frascati, I-00044 Frascati, Italy

[19b]INFN and University of Perugia, I-06100 Perugia, Italy

[20]Johannes Gutenberg University of Mainz, Johann-Joachim-Becher-Weg 45, D-55099 Mainz, Germany

[21]Joint Institute for Nuclear Research, 141980 Dubna, Moscow region, Russia

[22]KVI, University of Groningen, NL-9747 AA Groningen, The Netherlands

[23]Lanzhou University, Lanzhou 730000, People's Republic of China

[24]Liaoning University, Shenyang 110036, People's Republic of China

[25]Nanjing Normal University, Nanjing 210023, People's Republic of China

[26]Nanjing University, Nanjing 210093, People's Republic of China

[27]Nankai university, Tianjin 300071, People's Republic of China

[28]Peking University, Beijing 100871, People's Republic of China

[29]Seoul National University, Seoul 151-747 Korea

[30]Shandong University, Jinan 250100, People's Republic of China

[31]Shanxi University, Taiyuan 030006, People's Republic of China

[32]Sichuan University, Chengdu 610064, People's Republic of China

[33]Soochow University, Suzhou 215006, People's Republic of China

[34]Sun Yat-Sen University, Guangzhou 510275, People's Republic of China

[35]Tsinghua University, Beijing 100084, People's Republic of China

[36a]Ankara University, Dogol Caddesi, 06100 Tandogan, Ankara, Turkey

[36b]Dogus University, 34722 Istanbul, Turkey

[36c]Uludag University, 16059 Bursa, Turkey

[37]Universitaet Giessen, D-35392 Giessen, Germany

[38]University of Chinese Academy of Sciences, Beijing 100049, People's Republic of China

[39]University of Hawaii, Honolulu, Hawaii 96822, USA

[40]University of Minnesota, Minneapolis, Minnesota 55455, USA

[41]University of Rochester, Rochester, New York 14627, USA

[42]University of Science and Technology of China, Hefei 230026, People's Republic of China

[43]University of South China, Hengyang 421001, People's Republic of China

[44]University of the Punjab, Lahore-54590, Pakistan

[45a]University of Turin, I-10125 Turin, Italy

[45b]University of Eastern Piedmont, I-15121 Alessandria, Italy

[45c]INFN, I-10125 Turin, Italy

[46]Uppsala University, Box 516, SE-75120 Uppsala, Sweden

[47]Wuhan University, Wuhan 430072, People's Republic of China

[48]Zhejiang University, Hangzhou 310027, People's Republic of China

[49]Zhengzhou University, Zhengzhou 450001, People's Republic of China

We perform an analysis of the $D^+ \to K_S^0 \pi^+ \pi^0$ Dalitz plot using a data set of 2.92 fb^{-1} of e^+e^- collisions at the $\psi(3770)$ mass accumulated by the BESIII experiment, in which 166694 candidate events are selected with a background of 15.1%. The Dalitz plot is found to be well represented by a combination of six quasi-two-body decay channels $[K_S^0 \rho^+, K_S^0 \rho(1450)^+, \bar{K}^{*0} \pi^+, \bar{K}_0(1430)^0 \pi^+, \bar{K}(1680)^0 \pi^+, \bar{\kappa}^0 \pi^+]$ plus a small nonresonant component. Using the fit fractions from this analysis, partial branching ratios are updated with higher precision than previous measurements.

[*]Also at the Novosibirsk State University, Novosibirsk 630090, Russia.

[†]Also at the Moscow Institute of Physics and Technology, Moscow 141700, Russia.

[‡]Also at University of Texas at Dallas, Richardson, Texas 75083, USA.

[§]Also at the PNPI, Gatchina 188300, Russia.

I. INTRODUCTION

A clear understanding of final-state interactions in exclusive weak decays is an important ingredient in our ability to predict decay rates and to model the dynamics of

two-body decays of charmed mesons. Final-state interactions can cause significant changes in decay rates, and can cause shifts in the phases of decay amplitudes. Clear experimental measurements can help refine theoretical models of these phenomena.

Three-body decays provide a rich laboratory in which to study the interferences between intermediate-state resonances. They also provide a direct probe of final-state interactions in certain decays. When a particle decays into three or more daughters, such as the decay of $D \to P_1 P_2 P_3$, where P_i ($i = 1, 2, 3$) represents a pseudoscalar particle, intermediate resonances dominate the decay rate. Amplitudes are typically obtained with a Dalitz plot analysis technique [1], which uses the minimum number of independent observable quantities, and any variation in the population over the Dalitz plot shows dynamical rather than kinematical effects. This provides the opportunity to experimentally measure both the amplitudes and phases of the intermediate decay channels, which in turn allows us to deduce their relative branching fractions. These phase differences can even allow details about very broad resonances to be extracted by observing their interference with other intermediate states.

A large contribution from a $K\pi$ S-wave intermediate state has been observed in earlier experiments including MARKIII [2], NA14 [3], E691 [4], E687 [5], E791 [6,7], and CLEO-c [8] in the $D^+ \to K^-\pi^+\pi^+$ decay. Both E791 and CLEO-c interpreted their data with a model-independent partial wave analysis (MIPWA) and found a phase shift at low $K\pi$ mass to confirm the $\bar{\kappa}\pi$ component. Complementary to $D^+ \to K^-\pi^+\pi^+$, the $D^+ \to K^0_S\pi^+\pi^0$ decay is also a golden channel to study the $K\pi$ S-wave in D decays.

The previous Dalitz plot analysis of $D^+ \to K^0_S\pi^+\pi^0$ by MARKIII [2] included only two intermediate decay channels, $K^0_S\rho$ and $\bar{K}^{*0}\pi^+$, and was based on a small data set. A much larger data sample of e^+e^- collisions at $\sqrt{s} \approx 3.773$ GeV has been accumulated with the BESIII detector running at the Beijing Electron-Positron Collider (BEPCII). With much larger statistics, it is possible to measure relative branching fractions more precisely and to find more intermediate resonances. In this paper, we present an improved Dalitz plot analysis of the $D^+ \to K^0_S\pi^+\pi^0$ decay.

II. EVENT SELECTION

This analysis is based on a data sample of 2.92 fb^{-1} [9], which was collected at the peak of the $\psi(3770)$ resonance. BEPCII/BESIII [10] is a major upgrade of the BESII experiment at the BEPC accelerator [11]. The design peak luminosity of the double-ring e^+e^- collider, BEPCII [12], is 10^{33} cm^{-2} s^{-1} at a beam current of 0.93 A. The BESIII detector with a geometrical acceptance of 93% of 4π consists of the following main components: (1) a small-celled, helium-based main drift chamber with 43 layers. The average single wire resolution is $135\,\mu$m, and the

momentum resolution for a 1 GeV/c charged particle in a 1 T magnetic field is 0.5%. The chamber also provides a measurement of the specific energy loss dE/dx for charged particles; (2) an electromagnetic calorimeter (EMC) made of 6240 CsI(Tl) crystals arranged in a cylindrical shape (barrel) plus two end caps. For 1.0 GeV photons, the energy resolution is 2.5% in the barrel and 5% in the end caps, and the position resolution is 6 mm in the barrel and 9 mm in the end caps; (3) a time-of-flight system (TOF) for particle identification (PID) composed of a barrel part made of two layers with 88 pieces of 5 cm thick, 2.4 m long plastic scintillators in each layer, and two end caps with 96 fan-shaped, 5 cm thick, plastic scintillators in each end cap. The time resolution is 80 ps in the barrel, and 110 ps in the end caps, corresponding to better than a 2σ K/π separation for momenta below about 1 GeV/c; (4) a muon chamber system made of 1000 m^2 of resistive plate chambers arranged in nine layers in the barrel and eight layers in the end caps and incorporated in the return iron of the superconducting magnet. The position resolution is about 2 cm.

At the $\psi(3770)$, D mesons are produced in the reaction $e^+e^- \to \psi(3770) \to D\bar{D}$. A single D^+ (or D^-) is first reconstructed by its daughters. This analysis uses the $D^+ \to K^0_S\pi^+\pi^0$ decay and its charge conjugate channel. If one event contains both a D^+ and a D^- candidate, it will be treated as two events.

K^0_S candidates are detected through the decay $K^0_S \to \pi^+\pi^-$. The pions from the K^0_S are identified by requiring their dE/dx be within 4σ of the pion hypothesis. In order to improve the signal-to-background ratio, the decay vertex of $\pi^+\pi^-$ pairs is required to be more than 2 standard deviations in the measurement of the decay length away from the interaction point, and their invariant mass is required to be within 20 MeV of the mass of the K^0_S. They are then kinematically constrained to the K^0_S mass.

Charged π candidates are required to satisfy $|\cos\theta| < 0.93$, where θ is the polar angle with respect to the beam, to ensure reliable main drift chamber measurements. Only the tracks with points of closest approach to the beam line that are within 10 cm of the interaction point in the beam direction, and within 1 cm in the plane perpendicular to the beam, are selected. TOF and dE/dx information are combined to form PID confidence levels for π and K hypotheses. Pions are identified by requiring the pion probability to be larger than that for a kaon.

π^0 candidates are detected through the decay $\pi^0 \to \gamma\gamma$. Energy deposited in the nearby TOF counters is included in the photon energy measurement to improve the reconstruction efficiency and energy resolution [13]. Photon candidates in the barrel region ($|\cos\theta| < 0.8$, where θ is the polar angle of the shower) of the EMC must have at least 25 MeV total energy deposition; those in the end cap region ($0.84 < |\cos\theta| < 0.92$) must have at least 50 MeV total energy deposition. All neutral
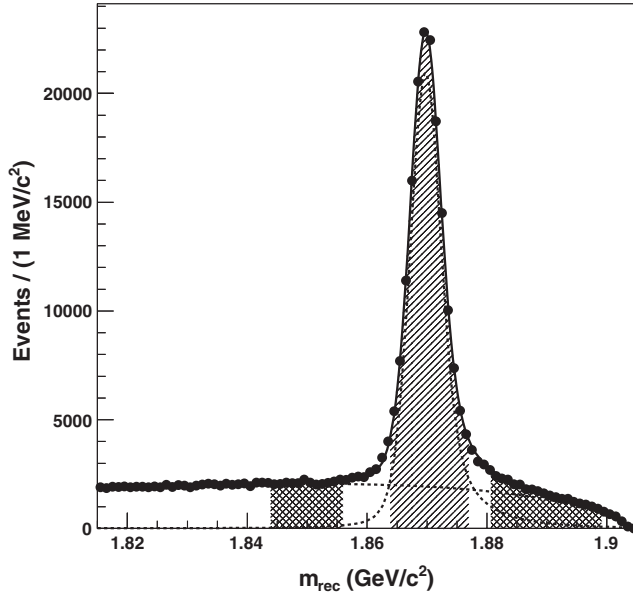
FIG. 1.   The recoil-mass distribution of $K^0_S\pi^+\pi^0$ candidates.

FIG. 2.   (a) The Dalitz plot for data and the projections onto (b) $m^2_{\pi^+\pi^0}$, (c) $m^2_{K^0_S\pi^0}$, and (d) $m^2_{K^0_S\pi^+}$.

showers must lie in a window of EMC time measured by the rising edge of the signal in the preamplifier electronics to reduce the number of fake π^0 from random electronics noise and to improve their resolution. Of each $\gamma\gamma$ pair, at least one γ is required to be in the barrel EMC, and the $\gamma\gamma$ mass is required to satisfy $0.115\text{ GeV} < m(\gamma\gamma) < 0.150\text{ GeV}$. The pair is then kinematically constrained to the π^0 mass.

After K^0_S, π^+ and π^0 candidates are selected, D^+ candidates are constructed using the requirement $-73\text{ MeV} < \Delta E < 41\text{ MeV}$, where $\Delta E = E_D - E_b$, E_D is the sum of the K^0_S, π^+ and π^0 candidate energies, and E_b is the beam energy, in the center mass system of e^+e^-. For multiple D^+ candidates, the candidate with the smallest $|\Delta E|$ is chosen. We then perform a kinematic fit in which the invariant mass of the D^+ candidate is constrained to the D^+ mass, and its recoiling mass $m_{rec} = \sqrt{(\mathbf{p}_{e^+e^-} - \mathbf{p}_D)^2}$ is allowed to vary, where $\mathbf{p}_{e^+e^-}$ is the four-momentum of the e^+e^- system and $\mathbf{p}_D$ is the four-momentum of the reconstructed D^+ candidate. This ensures that all D^+ decays have the same amount of phase space, regardless of whether the recoiling mass is in the signal or sideband region.

Figure 1 shows the recoil-mass distribution fitted with a signal shape derived from Monte Carlo (MC) simulation [14], with an ARGUS function [15] for the combinatorial background. The signal shape is determined by the MC shape convolved with a Gaussian resolution function. The signal region is defined as $1.864\text{ GeV} < m_{rec} < 1.877\text{ GeV}$, corresponding to the shaded region of Fig. 1; the events in the cross-hatched regions are taken as sideband events. In the signal region, the number of events above the combinatorial background is determined to be 142446 ± 378, and
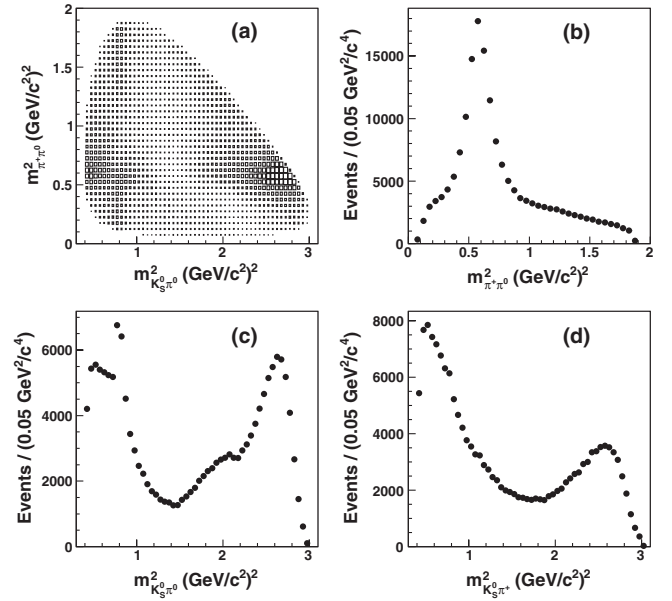
the amount of background in the signal region is estimated to be 24248 ± 156 events. Therefore, the size of the signal in the signal region is $(85.45 \pm 0.09)\%$ of the total. A peaking background contribution is included in the signal shape, which accounts for self-cross-feed events (where the D^+ decays to $K^0_S\pi^+\pi^0$, but the two π^+ are swapped, one from the D^+ and one from the K^0_S). The size of the peaking background is estimated using a MC study to be about 0.6% of the signal size. Subtracting this background, the signal purity is $(84.9 \pm 0.1)\%$.

Figure 2 shows the Dalitz plot of the selected data sample in the signal region and three projections onto the squared $K^0_S\pi^0$ invariant mass ($m^2_{K^0_S\pi^0}$), the squared $\pi^+\pi^0$ invariant mass ($m^2_{\pi^+\pi^0}$), and the squared $K^0_S\pi^+$ invariant mass ($m^2_{K^0_S\pi^+}$). In this paper, $x = m^2_{K^0_S\pi^0}$ and $y = m^2_{\pi^+\pi^0}$ are selected as the two axes of the Dalitz plot, since only two of these three variables are independent according to energy and momentum conservation; $m^2_{K^0_S\pi^+}$ is defined as z.

III. PARTIAL WAVE ANALYSIS

A. Matrix element

The $D^+ \to K^0_S\pi^+\pi^0$ Dalitz plot distribution satisfies $d\Gamma/dxdy \propto |\mathcal{M}|^2$, where $\mathcal{M}$ is the decay matrix element and contains the dynamics. The matrix element is parametrized by

$$\mathcal{M} = \sum_{L=0}^{L_{max}} Z_L F^L_D A_L, \tag{1}$$

where Z_L describes the angular distribution of the final-state particles; F_D^L is the barrier factor for the production of the partial wave; and A_L is the partial wave. The sum is over the decay orbital angular momentum L of two-body partial waves. In this analysis we consider the sum up to the maximal orbital momentum $L_{\max} = 3$.

The partial waves A_L are L-dependent functions of a single variable s_R (x, y, or z). In the $D^+ \to K_S^0 \pi^+ \pi^0$ decay, the S, P, D and F waves ($L = 0, 1, 2, 3$ respectively) are represented by the sum of functions $\mathcal{W}_R$ for individual intermediate states:

$$A_0(x) = c_{NR} + \mathcal{W}_{\bar{\kappa}^0} + \mathcal{W}_{\bar{K}_0^*(1430)^0}$$
$$+ (\mathcal{W}_{\kappa^+} + \mathcal{W}_{K_0^*(1430)^+})_{\text{DCS}}, \qquad (2a)$$

$$A_1(x) = \mathcal{W}_{\bar{K}^{*0}} + \mathcal{W}_{\bar{K}^*(1410)^0} + \mathcal{W}_{\bar{K}^*(1680)^0}$$
$$+ (\mathcal{W}_{K^{*+}} + \mathcal{W}_{K^*(1410)^+} + \mathcal{W}_{K^*(1680)^+})_{\text{DCS}}, \qquad (2b)$$

$$A_1(y) = \mathcal{W}_\rho + \mathcal{W}_{\rho(1450)}, \qquad (2c)$$

$$A_2(x) = \mathcal{W}_{\bar{K}_2^*(1430)^0} + (\mathcal{W}_{K_2^*(1430)^+})_{\text{DCS}}, \qquad (2d)$$

and

$$A_3(x) = \mathcal{W}_{\bar{K}_3^*(1780)^0} + (\mathcal{W}_{K_3^*(1780)^+})_{\text{DCS}}, \qquad (2e)$$

where the subscripts denote the intermediate resonances (expressed by R generally), and those in doubly Cabbibo suppressed (DCS) channels are marked out. The contribution of nonresonant (NR) decays is represented by $c_{\text{NR}} = a_{\text{NR}} e^{i\phi_{\text{NR}}}$, a complex factor with two fit parameters for magnitude a_{NR} and phase ϕ_{NR}. For each resonance, the function

$$\mathcal{W}_R = c_R W_R F_R^L \qquad (3)$$

is the shape of an individual resonance, W_R, multiplied by the barrier factor in the resonance R decay vertex, F_R^L, and the coupling factor, $c_R = a_R e^{i\phi_R}$.

In this analysis, the angular distribution Z_L, the barrier factor F_D^L (F_R^L), and the resonance dynamical function W_R are chosen as described in Appendix A.

B. Maximum likelihood fit

In order to describe the event density distribution on the Dalitz plot we use a probability density function (p.d.f.) $\mathcal{P}(x, y)$ described as follows:

$$\mathcal{P}(x, y) = \begin{cases} \dfrac{\varepsilon(x,y)|\mathcal{M}(x,y)|^2}{\int_{\text{DP}} \varepsilon(x,y)|\mathcal{M}(x,y)|^2 dxdy} & \text{for efficiency,} \\[3mm] \dfrac{B_1(x,y)}{\int_{\text{DP}} B_1(x,y)dxdy} & \text{for background, and} \\[3mm] f_S \dfrac{|\mathcal{M}(x,y)|^2\varepsilon(x,y)}{\int_{\text{DP}}|\mathcal{M}(x,y)|^2\varepsilon(x,y)dxdy} + f_{B1}\dfrac{B_1(x,y)}{\int_{\text{DP}}B_1(x,y)dxdy} + f_{B2}\dfrac{B_2(x,y)}{\int_{\text{DP}}B_2(x,y)dxdy} & \text{for signal with background,} \end{cases} \qquad (4)$$

where the $\varepsilon(x, y)$, $B_1(x, y)$, and $B_2(x, y)$ are functions representing the shapes of the efficiency, combinatorial background, and peaking background across the Dalitz plot, respectively; f_S, f_{B1}, and f_{B2} are the fractions of signal, combinatorial background and peaking background under the constraint that $f_S + f_{B1} + f_{B2} \equiv 1$; and the integral limit DP denotes the kinematic limit of the Dalitz plot. The p.d.f. free parameters are optimized with a maximum likelihood fit, where the log-likelihood function is described as

$$\ln \mathcal{L} = \sum_{i=1}^N \ln \mathcal{P}(x_i, y_i), \qquad (5)$$

where N is the number of events in the sample to parametrize.

Since we will test different models and obtain different parameters from different fits, we choose the Pearson goodness of fit to check them. A χ^2 variable for the multinomial distribution on the binned Dalitz plot is defined as

$$\chi^2 = \sum_{i=1}^N \frac{(n_i - v_i)^2}{v_i}, \qquad (6)$$

where N is the number of the bins, n_i is the number of events observed in the ith bin, and v_i is the number predicted from the fitted p.d.f.

C. Fit fractions

We calculate the contribution of each component in the matrix element using a standard definition of the fit fraction,

$$FF_C = \frac{\int_{\text{DP}} |\sum_{i \in C} \mathcal{A}_i(x, y)|^2 dxdy}{\int_{\text{DP}} |\mathcal{M}(x, y)|^2 dxdy}, \qquad (7)$$

where $\mathcal{A}_i(x, y)$ is the amplitude contribution of the ith component, described as $c_R Z_L F_D^L F_R^L W_R$ for resonances and c_{NR} for the nonresonant component, and C is any combined set of components. When C includes only one element, Eq. (7) gives the fit fraction of a single component.

For the $K_S^0\pi^0$ S-wave, it consists of a nonresonant piece, a $K_0^*(1430)^0$, and a κ^0.

D. Parameters

In Eq. (5), parameters include the ratios of signal and backgrounds, parameters describing the shapes of the efficiency and backgrounds, the coupling factors, the masses and widths of resonances, and the effective radii. Parameters for the efficiency shape are determined by studies of MC samples, and the backgrounds are estimated with the m_{rec} sideband events of data. They are fixed in the fit to data. The ratios of signal and backgrounds are also fixed by first fitting the m_{rec} distribution and studying the signal MC samples. The complex coupling factors, including the magnitude and phase, are free parameters in the fit and are used to calculate the fit fractions, but the magnitude and phase of the $K_S^0\rho^+$ component (which has the largest fit fraction) are fixed as 1 and 0. The masses and widths of the κ and the $K_0^*(1430)$ are allowed to vary. Those of the other resonances used in the fit are fixed to their PDG [16] values. The effective radii for the barrier factors are fixed at $r_D = 5.0$ GeV^{-1} and $r_R = 1.5$ GeV^{-1}.

IV. FITTING PROCEDURE

A. Efficiency

We determine the efficiency for signal events as a function of position in the two-dimensional Dalitz plot, which can be described as a product of a polynomial function and threshold factors:

$$\epsilon(x,y) = T(v)(1 + E_x x + E_y y + E_{xx}x^2 + E_{xy}xy + E_{yy}y^2$$
$$+ E_{xxx}x^3 + E_{xxy}x^2 y + E_{xyy}xy^2 + E_{yyy}y^3), \quad (8)$$

where $T(v)$ are the threshold factors for each Dalitz plot variable $v(x, y \text{ or } z)$, defined with an exponential form

$$T(v) = E_{0,v} + (1 - E_{0,v})[1 - e^{-E_{\text{th},v}|v - v_{\text{edge}}|}]. \quad (9)$$

All polynomial coefficients E_x, E_y, E_{xx}, E_{xy}, E_{yy}, E_{xxx}, E_{xxy}, E_{xyy}, and E_{yyy} are fit parameters. In the threshold function, the parameter $E_{\text{th},v}$ is free in the fit and v_{edge} is defined as the expected value of v at the Dalitz plot edge. E_0 denotes the efficiency when $v = v_{\text{max}}$. The threshold factor describes the low efficiency in regions with $v \to v_{\text{max}}$, where one of the three particles is produced with zero momentum in the D meson rest frame. We consider the threshold for $v = m_{K_S^0\pi^0}^2$ and $v = m_{\pi^+\pi^0}^2$.

To determine the efficiency we use a signal MC simulation [14] in which one of the charged D mesons decays in the signal mode, while the other D meson decays in all its known decay modes with proper branching fractions. These events are input into the BESIII detector simulation and are processed with the regular reconstruction package. The MC-generated events

are required to pass the same selection requirements as data in the signal region, as shown in Fig. 1. A track-matching technology is applied to the MC events to select only the signal mode side and to avoid contamination from the other D meson. Then the efficiency is obtained by fitting Eq. (4) to this sample with fixed $\mathcal{M}(x, y)$.

B. Background

As described in Sec. II, there are both combinatorial and peaking backgrounds. For the peaking background, the shape in the Dalitz plot is estimated by an MC sample, as shown in Fig. 3. Most of the self-cross-feed events have small $m_{K_S^0\pi^+}^2$ values, corresponding to small angles between the K_S^0 and the π^+. For the self-cross-feed contribution to the background, we use the histogram as the p.d.f. of $B_2(x, y)$. For the combinatorial background, we use data events from the two m_{rec} sideband regions, shown by the hatched range in Fig. 1.

Because the high-mass m_{rec} sideband has a significant contribution from signal events due to a tail caused by initial state radiation, we consider a contribution of signal for these events, whose fraction is obtained by fitting the distribution of m_{rec}. The contribution of signal, $\mathcal{M}_0$, is initialized by the parametrized shape of the low-mass sideband, $\mathcal{B}_0$. The $\mathcal{B}_0$ is fitted by Eq. (4) for background using events in the low-mass sideband, and then the $\mathcal{M}_0$ is fitted using $\mathcal{B}_0$ as $B_1(x, y)$. After that, the events in both sidebands are used to estimate the shape of the background in the Dalitz plot. $\mathcal{B}_1$ is parametrized to the total background events in sidebands by Eq. (4) for signal with background, based on the fixed $\mathcal{M}_0$, and then the $\mathcal{M}_1$ is fitted using $\mathcal{B}_1$. In order to make sure the right resonance contribution is used, this process is repeated i times to
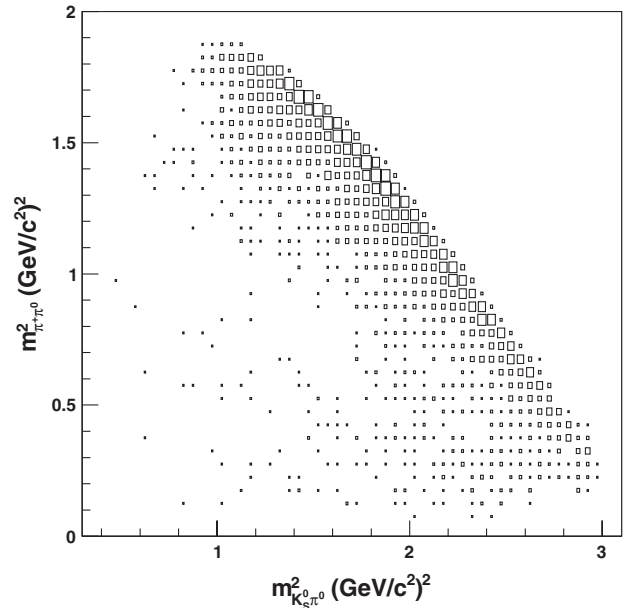

FIG. 3.   The shape of self-cross-feed events on the Dalitz plot.

obtain $\mathcal{B}_i$ and $\mathcal{M}_i$ until the variation of the signal from the last result is small enough. In this analysis, this process is repeated once.

The dominant misreconstructed D decays are from $D^+ \to K_S^0 a_1(1260)^+$, $D^0 \to K^- \pi^+ \pi^0$, and $D^0 \to K_S^0 \pi^+ \pi^- \pi^0$. It is worth noting that the background from the D^0 decay will bring a $K^*(892)^+$ contribution to the Dalitz plot which is a DCS process in the $D^+ \to K_S^0 \pi^+ \pi^0$ decay. We take this into account by adding this noncoherent $K^*(892)^+$ contribution to the background p.d.f., along with the $\rho(770)^+$ and $K^*(892)^0$ described below.

To parametrize the background shape on the Dalitz plot we employ a function similar to that used for the efficiency:

$$B_1(x, y) = T(x)(1 + B_x x + B_y y + B_{xx} x^2 + B_{xy} xy + B_{yy} y^2$$
$$+ B_{xxx} x^3 + B_{xxy} x^2 y + B_{xyy} xy^2 + B_{yyy} y^3$$
$$+ B_\rho |\mathcal{A}_\rho|^2 + B_{\bar{K}^{*0}} |\mathcal{A}_{\bar{K}^{*0}}|^2 + B_{K^{*+}} |\mathcal{A}_{K^{*+}}|^2), \quad (10)$$

where all the coefficients, B_x, B_y, B_{xx}, B_{xy}, B_{yy}, B_{xxx}, B_{xxy}, B_{xyy}, B_{yyy}, B_ρ, $B_{\bar{K}^{*0}}$, and $B_{K^{*+}}$, are fit parameters. Unlike the efficiency parametrization, the terms for the intermediate resonances ρ and $\bar{K}^{*0}$ describe the contributions from these resonances. Figure 4 shows the results of the fit with the background-corrected polynomial function to our sideband sample. There are some deviations between the parametrized functions and the sidebands, which primarily
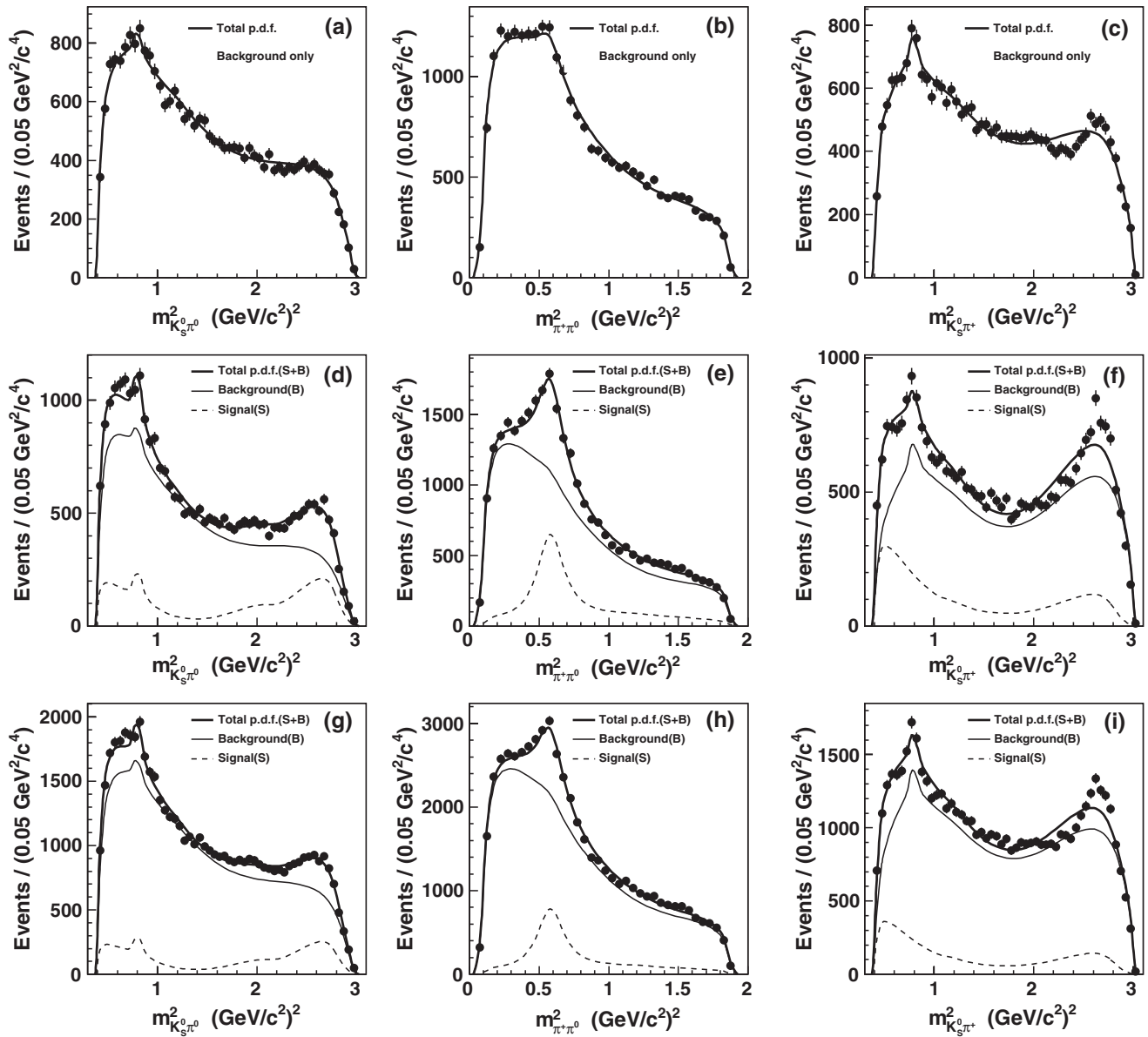

FIG. 4.   Results of the fit to the sideband backgrounds: (a), (b), and (c) are the three projections for the low-mass sideband only; (d), (e), and (f) are for the high-mass sideband only; and (g), (h), and (i) are for the combined sidebands. The signals are fed in for the signal tail in the sideband of the $m_{\rm rec}$ distribution.

TABLE I.   The intermediate resonance decay modes considered in this analysis.

CF mode		DCS mode
$K_S^0 X^+$	$X^0 \pi^+$	$X^+ \pi^0$
$K_S^0 \rho(770)^+$	$\bar{K}^*(892)^0 \pi^+$	$K^*(892)^+ \pi^0$
$K_S^0 \rho(1450)^+$	$\bar{K}_0^*(1430)^0 \pi^+$	$K_0^*(1430)^+ \pi^0$
	$\bar{K}^*(1680)^0 \pi^+$	$K^*(1680)^+ \pi^0$
	$\bar{\kappa}^0 \pi^+$	$\kappa^+ \pi^0$
$K_S^0 \rho(1700)^+$	$\bar{K}^*(1410)^0 \pi^+$	$K^*(1410)^+ \pi^0$
	$\bar{K}_2^*(1430)^0 \pi^+$	$K_2^*(1430)^+ \pi^0$
	$\bar{K}_3^*(1780)^0 \pi^+$	$K_3^*(1780)^+ \pi^0$

lie on the projection of $m_{K_S^0 \pi^+}^2$. The deviations will be considered as one source of systematic error in Sec. V A. The impact of the deviation is comparable to other sources of systematic uncertainties.

C. Fit to data

A previous analysis from the MARKIII experiment [2] included only two intermediate resonances in the $D^+ \to K_S^0 \pi^+ \pi^0$ decay: $K_S^0 \rho^+$ and $\bar{K}^{*0} \pi^+$. Obvious contributions from more resonances have been seen in the more recent $D^+ \to K^- \pi^+ \pi^+$ analyses. Hence, more resonances are considered in this analysis. All possible intermediate resonance decay modes are listed in Table I, including Cabbibo favored (CF) modes and DCS modes. A model using only these CF channels is found to be adequate. No evidence is found for additional DCS channels. However, the heavy ρ mesons, $\rho(1450)$ and $\rho(1700)$, contribute parts of their resonance shapes, and then their shapes in the Dalitz plot are close. As pointed out by CLEO [17], the inclusion of both ρ resonances is probably a misrepresentation of the contents of the Dalitz plot. In order to avoid fake interference, we choose only one of them, the $\rho(1450)$, to express approximatively their combined contribution in the decay matrix element. The results of the CF model (called model A) with a complex pole for the κ and Breit-Wigner functions for the other resonances are listed in the column "Model A" of Table II.

Based on model A, we perform a fit with a model without the $\bar{\kappa}$ (called model B) as a test, as listed in the column "Model B" of Table II. It is found that the goodness of fit is worse than in model A, which demonstrates the presence of $\bar{\kappa}$ in our data at high confidence level.

Similarly, we also test the model without the nonresonant component (called model C), and the results are listed in the column "Model C" of Table II. The resulting χ^2 increases by 105 units over model A, indicating that a nonresonant component is indeed present in our data.

In the above three models, the contributions of the three channels $\bar{K}^*(1410)^0 \pi^+$, $\bar{K}_2^*(1430)^0 \pi^+$, and $\bar{K}_3^*(1780)^0 \pi^+$ are not significant, compared to the systematic uncertainties

estimated in model A (listed in Table II). Therefore, we remove them from model A as the final model (called model D). Model D is composed of a nonresonant component and intermediate resonances, including $K_S^0 \rho(770)^+$, $K_S^0 \rho(1450)^+$, $\bar{K}^*(892)^0 \pi^+$, $\bar{K}_0^*(1430)^0 \pi^+$, $\bar{K}^*(1680)^0 \pi^+$, and $\bar{\kappa}^0 \pi^+$. The results are listed in the column "Model D" of Table II. Except for the large ($\sim 85\%$) contributions from $K_S^0 \rho(770)^+$ and $K_S^0 \rho(1450)^+$, and a visible ($\sim 3\%$) component of $\bar{K}^{*0} \pi^+$, a significant ($\sim 20\%$) contribution of $K_S^0 \pi^0$ S-wave is found in our fit. The projections of the fit and the Dalitz plot are shown in Fig. 5.

A deviation of efficiency between data and MC simulation will cause a deviation of the fit results. Therefore, a momentum-dependent correction is applied to the final results. First, the differences of efficiencies between MC and data are determined. For the charged π tracking efficiency and PID, Ref. [18] has studied their momentum-dependent differences through $\psi' \to \pi^+ \pi^- J/\psi$ and $J/\psi \to \rho \pi \to \pi^+ \pi^- \pi^0$. They are also studied using $D^0 \to K^- \pi^+$ and $D^+ \to K^- \pi^+ \pi^+$ control samples. The momentum-dependent differences in this range are all smaller than 2% and are used to correct MC efficiencies. The K_S^0 efficiency is studied through $J/\psi \to K^{*-} K^+$ and $D^0 \to K^{*-} \pi^+$ control samples. Besides the sample obtained by the standard selection, a loose selection without the K_S^0 requirement is used to obtain a reference sample. The distributions of missing mass squared of these K_S^0 are fitted with the shape of MC signal convolved by a Gaussian function plus the shape of the MC backgrounds. The number of expected events $N_{\rm exp}$ is obtained from the reference sample, and the number of observed events $N_{\rm obs}$ from the standard sample. Then the efficiency is taken as $N_{\rm obs}/N_{\rm exp}$. Dividing the samples into subsamples according to momentum, momentum-dependent efficiencies are obtained. The same process is performed on data and MC events respectively, and their difference is shown in Fig. 6(a). The π^0 efficiency is studied through the $D^0 \to K \pi \pi^0$ control sample, and similar steps are taken. Figure 6(b) shows the difference in the π^0 reconstruction efficiency. According to the momentum-dependent differences, a correction is performed. Details of the correcting process are described in Appendix B. The corrected results of model D are listed in Table III.

In fits with these models, the $\bar{\kappa}$ is represented with a complex pole form, and the position of the pole κ is allowed to float as a free complex parameter. The pole of the κ is measured at $(752 \pm 15 \pm 69^{+55}_{-73}, -229 \pm 21 \pm 44^{+40}_{-55})$ MeV, where the errors are statistical, experimental, and modeling uncertainties, respectively, consistent with the model C result of CLEO-c [8].

The mass and width of the $K_0^*(1430)^0$ are also floated, since the measured values from E791 [6] and CLEO-c [8] in the $D^+ \to K^- \pi^+ \pi^+$ decay are significantly different from the measurement from the $K p$ experiment LASS [19]. In our fit, the mass and width of the $K_0^*(1430)^0$ are

TABLE II.   The results of the fits to the $D^+ \to K_S^0 \pi^+ \pi^0$ Dalitz plot with a complex pole for the κ and Breit-Wigner functions for others, described in the text. The first terms of errors are statistical and the second terms are experimental errors in model A, and statistical only in models B, C, and D. Model A includes all decay modes listed in the first column. Based on model A, model B excludes the contribution of $\bar{\kappa}^0 \pi^+$; model C excludes the nonresonant contribution; model D consists of the decay modes after dropping the modes with small fractions, $\bar{K}^*(1410)^0 \pi^+$, $\bar{K}_2^*(1430)^0 \pi^+$, and $\bar{K}_3^*(1780)^0 \pi^+$. The S-wave is calculated by adding the nonresonant component, the $\bar{\kappa}^0 \pi^+$, and the $\bar{K}_0^*(1430)^0 \pi^+$.

Decay mode	Parameters	Model A	Model B	Model C	Model D
Nonresonant	FF (%)	$4.5 \pm 0.7 \pm 2.6$	18.3 ± 0.6		6.1 ± 0.9
	$\phi(°)$	$269 \pm 6 \pm 26$	232.7 ± 1.3		276 ± 6
$K_S^0 \rho(770)^+$	FF (%)	$84.6 \pm 1.8 \pm 2.5$	82.0 ± 1.3	86.7 ± 1.1	82.2 ± 2.2
	$\phi(°)$	0 (fixed)	0 (fixed)	0 (fixed)	0 (fixed)
$K_S^0 \rho(1450)^+$	FF (%)	$1.8 \pm 0.2 \pm 0.8$	6.03 ± 0.29	0.63 ± 0.12	2.65 ± 0.28
	$\phi(°)$	$198 \pm 4 \pm 10$	167.1 ± 2.1	186 ± 8	183.7 ± 2.6
$\bar{K}^*(892)^0 \pi^+$	FF (%)	$3.22 \pm 0.14 \pm 0.15$	2.99 ± 0.10	3.30 ± 0.10	3.38 ± 0.16
	$\phi(°)$	$294.7 \pm 1.3 \pm 1.4$	279.3 ± 1.2	292.3 ± 1.5	292.2 ± 1.3
$\bar{K}^*(1410)^0 \pi^+$	FF (%)	$0.12 \pm 0.05 \pm 0.17$	0.18 ± 0.05	0.12 ± 0.05	
	$\phi(°)$	$228 \pm 9 \pm 26$	301 ± 10	243 ± 12	
$\bar{K}_0^*(1430)^0 \pi^+$	FF (%)	$4.5 \pm 0.6 \pm 1.2$	10.5 ± 1.3	3.6 ± 0.5	3.7 ± 0.6
	$\phi(°)$	$319 \pm 5 \pm 14$	306.2 ± 2.0	317 ± 4	339 ± 5
	Mass (MeV)	$1452 \pm 5 \pm 15$	1435 ± 4	1449 ± 4	1470 ± 6
	Width (MeV)	$184 \pm 7 \pm 15$	287 ± 11	163 ± 6	187 ± 7
$\bar{K}_2^*(1430)^0 \pi^+$	FF (%)	$0.12 \pm 0.02 \pm 0.09$	0.086 ± 0.014	0.111 ± 0.015	
	$\phi(°)$	$273 \pm 7 \pm 18$	265 ± 9	267 ± 7	
$\bar{K}^*(1680)^0 \pi^+$	FF (%)	$0.21 \pm 0.06 \pm 0.08$	0.58 ± 0.08	0.43 ± 0.10	1.05 ± 0.09
	$\phi(°)$	$243 \pm 6 \pm 22$	284 ± 4	234 ± 5	255.3 ± 2.0
$\bar{K}_3^*(1780)^0 \pi^+$	FF (%)	$0.034 \pm 0.008 \pm 0.020$	0.055 ± 0.008	0.037 ± 0.008	
	$\phi(°)$	$130 \pm 12 \pm 50$	113 ± 9	131 ± 11	
$\bar{\kappa}^0 \pi^+$	FF (%)	$6.8 \pm 0.7 \pm 2.2$		18.8 ± 0.5	6.4 ± 1.0
	$\phi(°)$	$92 \pm 6 \pm 22$		11.6 ± 1.9	92 ± 7
	$\Re$ (MeV)	$739 \pm 14 \pm 40$		773 ± 11	750 ± 15
	$\Im$ (MeV)	$-220 \pm 14 \pm 15$		-396 ± 18	-230 ± 21
$NR + \bar{\kappa}^0 \pi^+$	FF (%)	$18.1 \pm 1.4 \pm 1.6$	18.3 ± 0.6	18.8 ± 0.5	19.2 ± 1.8
$K_S^0 \pi^0$ S-wave	FF (%)	$18.9 \pm 1.0 \pm 2.0$	15.8 ± 1.0	21.2 ± 1.0	17.1 ± 1.4
ΣFF (%)		106	121	114	105
$\chi^2/Ndof$		1672/1187	2497/1191	1777/1189	2068/1193
$-2 \ln \mathcal{L}$		239415	240284	239521	239807

$1464 \pm 6 \pm 9^{+9}_{-28}$ MeV and $190 \pm 7 \pm 11^{+6}_{-26}$ MeV, respectively, consistent with the measurements from CLEO-c and E791. In our model without the $\bar{\kappa}$, the efficiency corrected results are 1444 ± 4 MeV and 283 ± 11 MeV, with statistical errors only.

D. Cross-check with MIPWA

The biggest issue of any Dalitz plot analysis is its model dependence. An attempt to mitigate the model dependence for the $D^+ \to K^- \pi^+ \pi^+$ decay under study is described in [7]. Here, we apply this model-independent partial wave analysis (MIPWA) technique as a cross-check of our model D for the contributions of $K_S^0 \pi^0$ S-wave.

The complex term $\mathcal{W}_R$ and c_{NR} in Eqs. (2) and (3) can be used alone or in combination with other terms. In this check, it represents a correction to the complex amplitude

of the isobar model. We use this term in the form of an s-dependent complex number,

$$\mathcal{W}_{L,\text{binned}}(s) = a_L(s) e^{i\varphi_L(s)}, \qquad (11)$$

with the functions $a_L(s)$ and $\varphi_L(s)$ calculated by a linear interpolation between the bins for the magnitude a_{Lk} and phase φ_{Lk}, where $k(s) = 1, 2, \ldots, N_L$ is an s-dependent index of these bins.

We test two models, one with a binned $K_S^0 \pi^0$ S-wave, and another with a binned $K_S^0 \pi^0$ S-wave excluding the $\bar{K}_0^*(1430)^0$ (whose contribution is kept in its Breit-Wigner form). The measured S-wave magnitudes and phases are illustrated in Fig. 7. In order to compare with the previous $D^+ \to K^- \pi^+ \pi^+$ results, we measure all magnitudes and phases relative to the $\bar{K}^*(892)^0 \pi^+$ decay mode in the MIPWA fits. Comparing the binned S-wave fit without
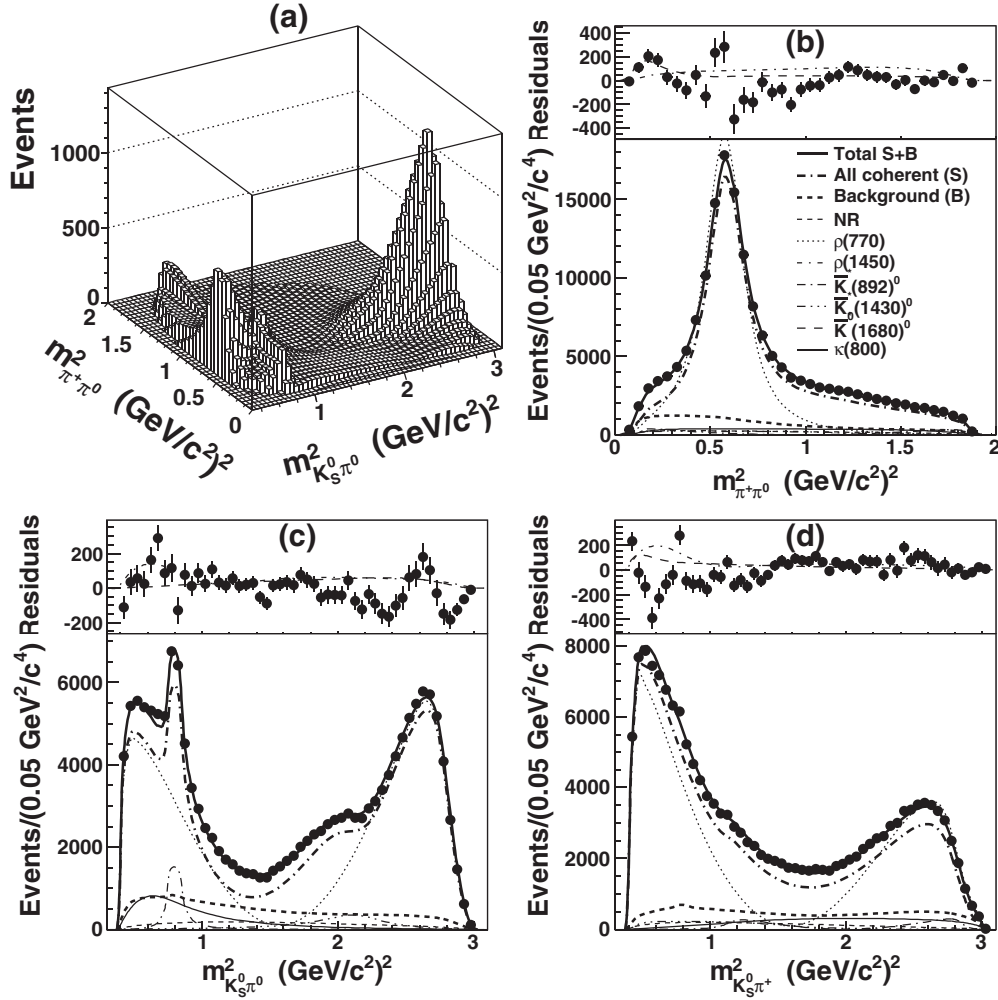
FIG. 5.   The results of fitting the $D^+ \to K_S^0 \pi^+ \pi^0$ data with model D. (a) Distribution of fitted p.d.f. and projections on (b) $m_{\pi^+\pi^0}^2$, (c) $m_{K_S^0\pi^0}^2$, and (d) $m_{K_S^0\pi^+}^2$. Residuals between the data and the total p.d.f. are shown by dots with statistical error bars in the top insets with minor contributions from the $\rho(1450)$ and the $\bar{K}^*(1680)^0$.

the $\bar{K}_0^*(1430)^0$ component to a sum of the $\bar{\kappa}$ pole and the nonresonant component in model D, and the total binned S-wave to a sum of the $\bar{\kappa}^0$ pole, $\bar{K}_0^*(1430)^0$ and the nonresonant component in model D, respectively, these models are consistent with the model-dependent analysis. It is obvious

that there is still a phase variation from low mass threshold to higher mass in the $K_S^0\pi^0$ S-wave excluding the $\bar{K}_0^*(1430)^0$, similar with the combination of the NR and the $\bar{\kappa}\pi^+$ in model D. In the total binned $K_S^0\pi^0$ S-wave, the amplitude is distorted by a contribution from the $\bar{K}_0^*(1430)$ resonance.
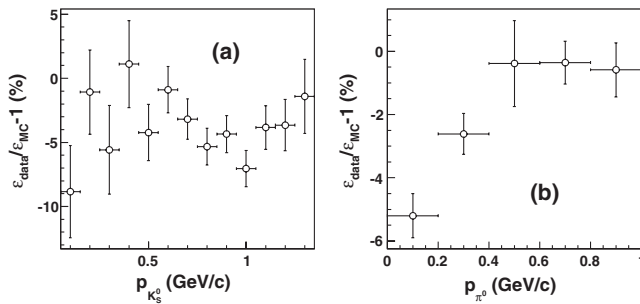
V. SYSTEMATIC UNCERTAINTIES

In our analysis, according to Eq. (4), there are several possible sources of systematic uncertainties: the background, the efficiency, the numerical integration, and the modeling of the decay. In order to estimate systematic uncertainties of the fit parameters due to these sources, we carry out the checks described in this section in detail. We require 10^{-8} precision to get the integral of the p.d.f. If we improve the precision by an order of magnitude, we find negligible change. The final systematic errors are shown in Table III. The "Total" experimental errors are obtained as a quadratic sum of that from background and efficiency.

FIG. 6.   The differences of efficiencies between data and MC as a function of momentum, (a) for K_S^0 and (b) for π^0, for the control samples described in the text.

TABLE III.   A summary of the statistical and systematic errors on the fit parameters of model D. The "Value" and "Statistical" columns show the results from the momentum-dependent efficiency correction. The three columns under "Experimental Errors" ("Modeling Errors") summarize the systematic uncertainties due to experimental (modeling) sources respectively, described in the text in detail. The S-wave is calculated by adding the nonresonant component, the $\bar{\kappa}^0\pi^+$, and the $\bar{K}_0^*(1430)^0\pi^+$.

Parameters	Value	Statistical errors	Experimental errors			Modeling errors		
			Background	Efficiency	Total	Shape	Add	Total
NR FF (%)	4.6	0.7	3.5	1.0	3.6	$+2.9$ -1.5	$+2.7$ -3.3	$+4.0$ -3.6
NR phase (°)	279	6	5	15	15	$+6$ -25	$+22$ -12	$+23$ -27
$\rho(770)^+$ FF (%)	83.4	2.2	2.7	0.7	2.8	$+1.1$ -1.9	$+6.4$ -1.1	$+6.5$ -2.2
$\rho(1450)^+$ FF (%)	2.1	0.3	0.9	0.9	1.2	$+0.7$ -0.1	$+0.8$ -1.5	$+1.0$ -1.5
$\rho(1450)^+$ phase (°)	187	3	4	4	5	$+9$ -15	$+26$ -5	$+28$ -16
$\bar{K}^*(892)^0$ FF (%)	3.58	0.17	0.12	0.11	0.17	$+0.31$ -0.18	$+0.16$ -0.28	$+0.35$ -0.34
$\bar{K}^*(892)^0$ phase (°)	293	2	1	2	2	$+2$ -7	$+6$ -2	$+6$ -7
$\bar{K}_0^*(1430)^0$ FF (%)	3.7	0.6	0.6	0.5	0.8	$+0.4$ -0.3	$+0.7$ -0.8	0.8
$\bar{K}_0^*(1430)^0$ phase (°)	334	5	8	4	9	$+1$ -10	$+3$ -28	$+3$ -30
$\bar{K}^*(1680)^0$ FF (%)	1.3	0.2	0.6	0.2	0.7	$+0.6$ -0.1	$+0.1$ -1.1	$+0.6$ -1.1
$\bar{K}^*(1680)^0$ phase (°)	252	2	9	6	11	$+6$ -2	$+7$ -28	$+9$ -28
$\bar{\kappa}^0$ FF (%)	7.7	1.2	2.5	3.1	4.0	$+2.0$ -2.7	$+4.7$ -0.1	$+5.1$ -2.7
$\bar{\kappa}^0$ phase (°)	93	7	25	14	28	$+14$ -7	$+16$ -22	$+21$ -23
$NR + \bar{\kappa}^0$ FF (%)	18.6	1.7	1.1	1.0	1.5	$+1.6$ -3.7	$+0.5$ -2.3	$+1.7$ -4.4
$K_S^0\pi^0$ S-wave FF (%)	17.3	1.4	2.1	0.5	2.1	$+0.7$ -3.8	$+2.6$ -0.6	$+2.7$ -3.8

A. Background

   The uncertainties from the background (shown in the "Background" column) come from two sources: the background shape and the background normalization. The
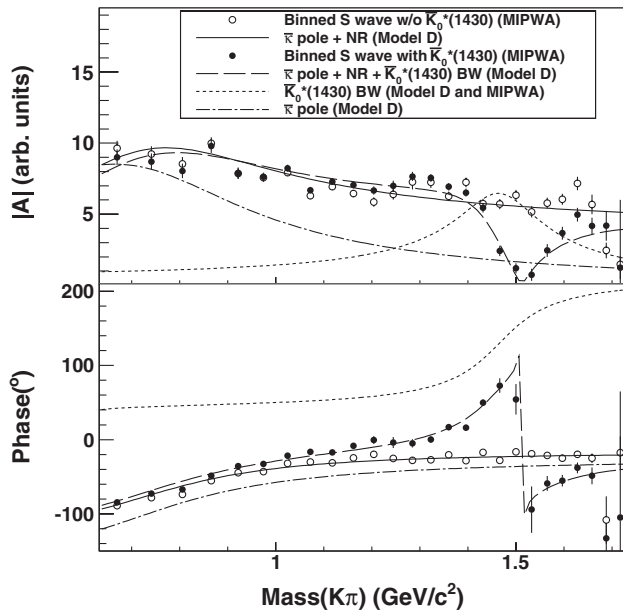

FIG. 7.   The magnitude and phase of the $K\pi$ S-wave in model D and the MIPWA. The open circles with error bars (statistical uncertainties only) show the binned $K\pi$ S-wave without the $K_0^*(1430)$ and the black dots show the total $K\pi$ S-wave. Other curves show the S-wave components of model D.

background shape depends on both the parametrization and the sideband approximation.

   There is a difference between the true background shape and the polynomial function as pointed out in Sec. IV B. But in the high-mass sideband, we do not know the shape of the background component because of the signal tail. According to Fig. 4, the differences are close in cases of low-mass sideband, high-mass sideband, and combined sideband. Hence, we choose the low-mass sideband to examine the 3rd order polynomial parametrization. Inputting the low-mass sideband shape using a histogram p.d.f., we compare to the fit result with the parametrized low-mass sideband shape. We take the variation as the systematic error.

   Both sidebands are used to parametrize background in the final fit, and it is believable that the deviation of this shape from the real background would not exceed the difference between backgrounds in the low-mass and high-mass sidebands. Inputting the background shape parametrized by these two sidebands, the difference of results is estimated as the uncertainty due to the background shape.

   In Sec. II, we estimate that the statistical error of the signal ratio is 0.1%. Through comparing MC truth to the result of fitting on the $m_{\rm rec}$ distribution of MC sample, its systematic uncertainty is estimated to be $^{+0.1}_{-1.4}$%, and if the signal ratio is floated in the Dalitz fit, the fitted value is (83.3 ± 0.4)%. They are consistent with each other. We change the signal ratio in the fit to change the background level by 1 standard deviation. The variation of results is taken as the estimation of uncertainty of the background level.

B. Efficiency

The systematic uncertainty from the efficiency (shown in the "Efficiency" column) includes two terms: the efficiency parametrization and the difference between data and MC. The sources of the difference of data and MC include event selection criteria, tracking, unstable particle reconstruction, and PID. The resolution of the detector is also considered here.

For the efficiency parametrization, we change the global polynomial fit to the average efficiencies of local bins. Each bin's efficiency value is replaced by the average efficiency. We also try smoothing the efficiencies by averaging either nine or twenty-five nearest neighbors as a check. The differences caused by using different parametrizations is also considered in the systematic error.

Another efficiency parametrization, which is obtained using a MC sample uniform in phase space, is used as a cross-check. The variation is taken as one of the systematic uncertainties.

Because the resolutions of ΔE and m_{rec} in data are a little larger than in MC, the efficiency shape could possibly be different as well. In order to estimate the uncertainty caused by the cuts, we change the cuts on the MC sample to make the cumulative probability at the cut position the same as data. This check indicates that this uncertainty is small.

The particle reconstruction and identification are also possible sources of systematic error. If the differences between data and MC are independent of three-momentum, there will be no effect on the relative branching fractions. Therefore, a momentum dependent correction on reconstruction and PID efficiency is performed, as described in Appendix B. Correspondingly, the rms of the measured values are taken as an estimate of the systematic errors.

To estimate the experimental systematic error due to the finite resolution of the Dalitz plot variables, we have included the effects of smearing when fitting the data as a check. This was done by measuring the resolution as a function of position across the Dalitz plot and numerically convoluting this with the amplitude at each point when performing the fit. The resulting change of parameters from the nominal best fit is very small and can be neglected when compared to other uncertainties.

C. Model

Systematic uncertainties of the modeling of the decay can arise from the parametrization of the resonances (shown in the "Shape" column), which include barrier factors, dynamical functions and resonance parameters, and also come from the choice of resonances in the baseline fit (shown in the "Add" column). The "Shape" and "Add" columns are added in quadrature to obtain the final model dependent systematic errors, shown in the "Total" column under "Modeling errors".

We test the exponential barrier factor $F_V^0 = e^{-(q^2-q_V^2)/12}$ as an alternative description of the scalar intermediate

resonances in Table V. A smaller NR fraction is obtained, but the total $K\pi$ S-wave is relatively unaffected. We do not consider it as a systematic error. We also test the fit by changing the radial parameters used in the barrier factors from 0 to 3 GeV^{-1} for the intermediate resonances, and from 0 to 10 GeV^{-1} for the D^+ meson. The maximum likelihood values $\mathcal{L}$ appear at $r_D \approx 2.75$ GeV^{-1} and $r_R \approx 1.48$ GeV^{-1}, respectively. It indicates that the radial parameter of the intermediate resonances is consistent with 1.5 GeV^{-1} and the radius of the D meson has large uncertainty. The variation caused by the uncertainties of the radii is taken as a systematic error.

Different resonance shapes for $\bar{K}_0^*(1430)$ and $\bar{\kappa}$ are tested. A Flatté form for $\bar{K}_0^*(1430)$ and Breit-Wigner for $\bar{\kappa}$ are tried. If only the $\bar{K}_0^*(1430)$ is changed to the Flatté form, the χ^2 changes by -11 units. If only the $\bar{\kappa}$ is changed to Breit-Wigner, the χ^2 changes by 11. We also perform the fit while floating the masses and widths of the $\rho(770)$ and the $\bar{K}^*(892)$. The variations from the nominal values are taken as an estimation of this systematic uncertainty.

The final systematic check is on our choice of which resonances are to be included. We do two fits for different $\rho(1450)^+$ and $\rho(1700)^+$, and take the variation of parameters as the error. We also add insignificant resonances one by one, including $\bar{K}^*(892)^+\pi^0$, $\bar{K}^*(1410)^0\pi^+$, $\bar{K}_0^*(1430)^+\pi^0$, $\bar{K}_2^*(1430)^0\pi^+$, $\bar{K}_3^*(1780)^0\pi^+$, and watch the variations of the fit fractions of the observed channels, which is taken as an additional systematic uncertainty.

VI. SUMMARY AND CONCLUSIONS

We describe an amplitude analysis of the $D^+ \to K_S^0 \pi^+ \pi^0$ Dalitz plot. We start with a BESIII data set of 2.92 fb^{-1} of e^+e^- collisions accumulated at the peak of the $\psi(3770)$, and select 166694 candidate events with a background of $(15.1 \pm 0.1^{+1.4}_{-0.1})\%$.

We fit the distribution of data to a coherent sum of six intermediate resonances plus a nonresonant component, with a low mass scalar resonance, the $\bar{\kappa}$, included. The final fit fraction and phase for each component is given in Table III. These fit fractions, multiplied by the world average $D^+ \to K_S^0 \pi^+ \pi^0$ branching ratio of $(6.99 \pm 0.27)\%$ [16], yield the partial branching fractions shown in Table IV. The error on the world average branching ratio is incorporated by adding it in quadrature with the experimental systematic errors on the fit fractions to give the experimental systematic error on the partial branching fractions.

In this result, the $K_S^0 \pi^0$ waves can be compared with the $K^-\pi^+$ waves in the $D^+ \to K^-\pi^+\pi^+$ decay. For example, according to our measured branching ratio of $D^+ \to \bar{K}^{*0}\pi^+ \to K_S^0\pi^+\pi^0$ and the PDG value of branching ratio of $D^+ \to \bar{K}^{*0}\pi^+ \to K^-\pi^+\pi^+$ of $(1.01 \pm 0.11)\%$, the ratio of the branching fractions of $D^+ \to \bar{K}^{*0}\pi^+ \to K^-\pi^+\pi^+$ and $D^+ \to \bar{K}^{*0}\pi^+ \to \bar{K}^0\pi^+\pi^0$ is calculated to be 2.02 ± 0.34, which is consistent with the expectation.

TABLE IV.   Partial branching fractions calculated by combining our fit fractions with the PDG's $D^+ \to K^0_S \pi^+ \pi^0$ branching ratio. The errors shown are statistical, experimental systematic, and modeling systematic, respectively.

Mode	Partial branching fraction (%)
$D^+ \to K^0_S \pi^+ \pi^0$ nonresonant	$0.32 \pm 0.05 \pm 0.25^{+0.28}_{-0.25}$
$D^+ \to \rho^+ K^0_S, \rho^+ \to \pi^+ \pi^0$	$5.83 \pm 0.16 \pm 0.30^{+0.45}_{-0.15}$
$D^+ \to \rho(1450)^+ K^0_S, \rho(1450)^+ \to \pi^+ \pi^0$	$0.15 \pm 0.02 \pm 0.09^{+0.07}_{-0.11}$
$D^+ \to \bar{K}^*(892)^0 \pi^+, \bar{K}^*(892)^0 \to K^0_S \pi^0$	$0.250 \pm 0.012 \pm 0.015^{+0.025}_{-0.024}$
$D^+ \to \bar{K}^*_0(1430)^0 \pi^+, \bar{K}^*_0(1430)^0 \to K^0_S \pi^0$	$0.26 \pm 0.04 \pm 0.05 \pm 0.06$
$D^+ \to \bar{K}^*(1680)^0 \pi^+, \bar{K}^*(1680)^0 \to K^0_S \pi^0$	$0.09 \pm 0.01 \pm 0.05^{+0.04}_{-0.08}$
$D^+ \to \bar{\kappa}^0 \pi^+, \bar{\kappa}^0 \to K^0_S \pi^0$	$0.54 \pm 0.09 \pm 0.28^{+0.36}_{-0.19}$
$NR + \bar{\kappa}^0 \pi^+$	$1.30 \pm 0.12 \pm 0.12^{+0.12}_{-0.30}$
$K^0_S \pi^0$ S-wave	$1.21 \pm 0.10 \pm 0.16^{+0.19}_{-0.27}$

We also apply a model-independent approach to describe the Dalitz plot, developed in Ref. [7], to confirm the results. The $K\pi$ S-wave can be well described by a $\bar{\kappa}$, a $\bar{K}^*_0(1430)$, and a nonresonant component. The resonance parameters of the κ and the $K^*_0(1430)$ are consistent with the results of E791 [6] and CLEO-c [8] in the $D^+ \to K^- \pi^+ \pi^+$ decay.

ACKNOWLEDGEMENTS

APPENDIX A: ISOBAR MODEL

In general, for the decay of $D \to Rc, R \to ab$, where the spins of a, b, and c are equal to zero, the orbital angular momentum between R and c is equal to the spin of R and the angular distribution can be simplified to a function of the momentum of a (p_a) and the momentum of c (p_c) in the R rest frame:

$$Z_L = (-2p_a p_c)^L P_L(\cos\theta), \tag{A1}$$

where the Legendre polynomials $P_L(\cos\theta)$ depend on the orbital angular momentum (the spin of R). Here θ is the helicity angle and its cosine is given in terms of the masses $m_a(m_c)$ and energies $E_a(E_c)$ of the $a(c)$ in the R rest frame:

$$\cos\theta = \frac{m_a^2 + m_c^2 + 2E_a E_c - m_{ac}^2}{2p_a p_c}. \tag{A2}$$

In this analysis, intermediate resonances are parametrized using the standard Breit-Wigner function defined as

$$W_R(m_{ab}) = \frac{1}{m_R^2 - m_{ab}^2 - im_R\Gamma(m_{ab})}, \tag{A3}$$

where m_R is the resonance mass and m_{ab} is the invariant mass of the ab system, and the mass-dependent width $\Gamma(m_{ab})$ has the usual form [20]:

$$\Gamma(m_{ab}) = \Gamma_R \left(\frac{p_a}{p_R}\right)^{2L+1} \left(\frac{m_R}{m_{ab}}\right) (F_R^L)^2, \tag{A4}$$

where Γ_R is the resonance width, and p_R is the value of p_a when $m_{ab} = m_R$.

In Eqs. (1), (3), and (A4), F_D^L and F_R^L are the barrier factors for the production of Rc and ab, defined using the Blatt-Weisskopf form [21], as listed in Table V.

For the $\bar{\kappa}$ we have tested both the Breit-Wigner function and the complex pole proposed in Ref. [22]:

$$W_R(m_{ab}) = \frac{1}{s_R - m_{ab}^2} = \frac{1}{m_R^2 - m_{ab}^2 - im_R\Gamma_R}, \tag{A5}$$

TABLE V. The Blatt-Weisskopf barrier factor used in this analysis. The index V stands for the D or R decay vertex, and $q = r_V p$ (p is the magnitude of the momentum of the decay daughters in the rest frame of mother particle, and r_V is the effective radius for the D or R vertex). For both D and R decays, $q_V = r_V p_V$, where p_V is the value of p when $m_{ab} = m_R$.

L	Form factor F_V^L
0	1
1	$\sqrt{\dfrac{1+q_V^2}{1+q^2}}$
2	$\sqrt{\dfrac{9+3q_V^2+q_V^4}{9+3q^2+q^4}}$
3	$\sqrt{\dfrac{405+45q_V^2+6q_V^4+q_V^6}{405+45q^2+6q^4+q^6}}$

which is equivalent to a Breit-Wigner function with constant width. In the fit,

$$s_R = (\Re + i\Im)^2, \tag{A6}$$

where $\Re$ and $\Im$ are the two parameters of the complex pole.

APPENDIX B: MOMENTUM-DEPENDENT CORRECTION

Based on momentum-dependent differences in efficiency, we can correct the MC efficiency to the expected data efficiency through a sampling method, and use the corrected efficiency to improve the results. The detailed steps are described as follows. First, an MC sample is generated and selected using the same event selection as data, and its events are denoted as $E_i(p_{K_S^0}, p_{\pi^+}, p_{\pi^0})$, $i = 1, \ldots, N$, where $p_{K_S^0}$, p_{π^+}, and p_{π^0} are the momentum of K_S^0, π^+, and π^0, respectively. Before sampling, the efficiency ratio of data and MC is computed as

$$r_\varepsilon(p_{K_S^0}, p_{\pi^+}, p_{\pi^0}) = \prod_c \frac{\varepsilon_{c,\text{data}}(p_c)}{\varepsilon_{c,\text{MC}}(p_c)}, \tag{B1}$$

where the subscripts c include the K_S^0 efficiency, the π^0 efficiency, the π^+ tracking efficiency, and the π^+ PID efficiency, and p_c denotes the momentum of the corresponding particles. Then for each event E_i, if r_ε is less than one, it will be compared with a uniform (0, 1) random number ζ, and the event is kept only if $r_\varepsilon > \zeta$; if r_ε is larger than one, the event will always be kept, and it will be repeated once while $r_\varepsilon - 1 > \zeta$. The sampling process is complete after all selected events are looped over. Finally, the efficiency parametrization is applied to the sampled events and the new efficiency parameters are used to fit data.

To remove the statistical fluctuations while sampling and the uncertainty of measurement of r_ε, we repeat this process, and change the r_ε value according to its uncertainty each time. Then we can obtain the distribution of results following a Gaussian distribution. The means denote the corrected results, and the sigmas describe the uncertainty of sampling and the measurement of efficiencies.

[1] R. H. Dalitz, Philos. Mag. **44**, 1068 (1953).

[2] J. Adler *et al.* (MARK-III Collaboration), Phys. Lett. B **196**, 107 (1987).

[3] M. P. Alvarez *et al.* (NA14/2 Collaboration), Z. Phys. C **50**, 11 (1991).

[4] J. C. Anjos *et al.* (E691 Collaboration), Phys. Rev. D **48**, 56 (1993).

[5] P. L. Frabetti *et al.* (E687 Collaboration), Phys. Lett. B **331**, 217 (1994).

[6] E. M. Aitala *et al.* (E791 Collaboration), Phys. Rev. Lett. **89**, 121801 (2002).

[7] E. M. Aitala *et al.* (E791 Collaboration), Phys. Rev. D **73**, 032004 (2006).

[8] G. Bonvicini *et al.* (CLEO Collaboration), Phys. Rev. D **78**, 052001 (2008).

[9] M. Ablikim *et al.* (BESIII Collaboration), Chin. Phys. C **37**, 123001 (2013).

[10] M. Ablikim *et al.* (BESIII Collaboration), Nucl. Instrum. Methods Phys. Res., Sect. A **614**, 345 (2010).

[11] J. Z. Bai *et al.* (BES Collaboration), Nucl. Instrum. Methods Phys. Res., Sect. A **344**, 319 (1994); (BES Collaboration) **458**, 627 (2001).

[12] F. A. Harris *et al.* (BES Collaboration), Nucl. Phys. B, Proc. Suppl. **162**, 345 (2006).

[13] M. He *et al.*, Chin. Phys. C **32**, 269 (2008).

[14] W. D. Li, H. M. Liu *et al.*, in *Proceedings of CHEP06, Mumbai, 2006*, edited by Sunanda Banerjee (Tata Institute of Fundamental Research, Mumbai, 2006).

[15] H. Albrecht *et al.* (ARGUS Collaboration), Phys. Lett. B **241**, 278(1990).

[16] J. Beringer *et al.* (Particle Data Group), Phys. Rev. D **86**, 010001 (2012).

[17] S. Kopp *et al.* (CLEO Collaboration), Phys. Rev. D **63**, 092001 (2001).

[18] M. Ablikim *et al.* (BESIII Collaboration), Phys. Rev. D **83**, 112005 (2011).

[19] D. Aston *et al.*, Nucl. Phys. B **296**, 493 (1988).

[20] H. Pilkuhn, *The Interactions of Hadrons* (North-Holland, Amsterdam, 1967).

[21] J. M. Blatt and V. F. Weisskopf, *Theoretical Nuclear Physics* (Wiley, New York, 1951).

[22] J. A. Oller, Phys. Rev. D **71**, 054030 (2005).